THE ASTROPHYSICAL JOURNAL, 466:135–149, 1996 July 20

H I AND THE MAFFEI 2 STARBURST: A MERGER SCENARIO

ROBERT L. HURT,[1,2] JEAN L. TURNER,[2] AND PAUL T. P. HO[3]
Received 1995 November 29; accepted 1996 February 6

ABSTRACT

We present high-resolution H I maps of the nearby starburst galaxy Maffei 2. These VLA maps have maximum resolutions of 20″ and show emission extending across 15′, well beyond the optical extent of the galaxy. The radio continuum emission matches the barred asymmetric morphology seen in the infrared. The asymmetries in the outer disk are also evident in H I, although the nucleus, which exhibits strong CO emission, is deficient in atomic gas. The total H I mass of the galaxy is $1.1 \times 10^9\ M_\odot$, accounting for ~1.5% of its total inferred dynamical mass. Its velocity field is, to first, order, typical of symmetrical barred galaxies, although there is a 10 km s^{-1} difference in systemic velocity between the disk and nucleus. Maffei 2 has a markedly disturbed appearance with an unusual H I "double arc" to the north that is probably a tidal feature indicating a recent or ongoing interaction. We propose that the asymmetries in the galaxy as well as its nuclear starburst are driven by an ongoing merger with a small satellite companion galaxy.

Subject headings: galaxies: individual (Maffei 2) — galaxies: interactions — galaxies: spiral — galaxies: starburst — galaxies: structure — radio lines: galaxies

1. INTRODUCTION

In recent years, the study of the starburst phenomenon has been a significant focus of extragalactic studies. Often starbursts are found in the inner nuclei of otherwise normal spiral galaxies, raising the primary dynamical question of how such nuclear bursts are fueled presumably from inflow of gas from the disk. Such "normal" starbursts are much more common than their ultraluminous kin, and accordingly may be found much closer to the Milky Way. With interferometers like the VLA, it is possible to examine in detail the structure and kinematics of these galaxies and derive a better understanding of how the global structure is related to the nuclear starbursts.

Maffei 2 is one of the nearest starburst galaxies, with nuclear star formation rates nearly as large as M83 and NGC 253 (Turner & Ho 1994; Ho, Beck, & Turner 1990). It is relatively close at 5 Mpc (Spinrad et al. 1973) and can be studied with high spatial resolution. Suffering from ~5 mag of visual extinction, it is often overlooked because of its location directly behind the Galactic plane ($l = 136°30'$, $b = -0°19'$). Maffei 2 was first noticed as an anomalous source on a near-infrared plate by Maffei (1968) along with its nearby companion Maffei 1. They were soon identified as spiral and elliptical galaxies, respectively (Spinrad et al. 1971). This region is one of growing interest as recent surveys of the "Zone of Avoidance" behind the disk of the Milky Way have identified several additional galaxies at similar distances within a few degrees of Maffei 1 and 2, qualifying this region as a small cluster in its own right (Kraan-Kortweg et al. 1994; Huchtmeier et al. 1995; McCall & Buta 1995).

We have mapped the H I emission in Maffei 2 to probe the large-scale gas structure and dynamics, looking for processes that might be driving the nuclear starburst. In § 2 we outline our observations and data reduction, including problems introduced by foreground Galactic H I emission. We discuss the morphologies and features of the continuum and integrated H I maps in §§ 3 and 4, respectively. Neutral gas kinematics and dynamical mass are covered in § 5. In § 6 we discuss the likelihood that the Maffei 2 morphological asymmetries and starburst are caused by a tidal interaction and discuss a possible scenario involving an ongoing merger with a companion galaxy, initially proposed on the basis of near-infrared observations (Hurt et al. 1993a).

2. OBSERVATIONS AND DATA REDUCTION

We observed Maffei 2 in the 21 cm neutral hydrogen (H I) emission line at 1420.406 MHz using the C and D configurations of the Very Large Array (VLA) of the NRAO.[4] The C configuration observations were made on 1985 September 3 and the D array on 1985 December 26. The resulting (u, v) baselines provide spatial sensitivities to structures of dimension ~15″ to 15′. The position of the nuclear radio continuum peak was chosen to be the phase center ($\alpha_{1950} = 2^h38^m08^s.50$, $\delta_{1950} = 59°23'30''.0$; Turner & Ho 1994). The phase calibrator was 0300+471, which had a flux density of 1.4 Jy and an absolute positional uncertainty of ~0″.1. Absolute fluxes were calibrated by adopting a value of 15.76 Jy for the source 3C 84 and are accurate to ~5%. The correlator setup was 64 channels in a single polarization mode, giving a per channel resolution of 48.828 kHz (10.3 km s^{-1} at 21 cm), across a total bandwidth of 3.1 MHz (660 km s^{-1}). The data were edited, calibrated, mapped, and CLEANed using the NRAO AIPS package. The presence of a strong, nearly pointlike continuum source at the phase center allowed the data from both configurations to be self-calibrated to compensate for phase errors.

Three different image cubes were constructed from the data to focus on different properties of the H I distribution. The "high-resolution" image, used for most of the figures in this paper, was constructed from the combined C and D

[1] Department of Physics, University of California at Riverside, Riverside, CA 92521.
[2] Department of Physics and Astronomy, UCLA, Los Angeles, CA 90095-1562.
[3] Center for Astrophysics, 60 Garden Street, Cambridge, MA 02138.

[4] The National Radio Astronomy Observatory is operated by Associated Universities, Inc., under cooperative agreement with the National Science Foundation.

configuration data using uniform weighting and a slight 8 kλ taper. The resulting restoring beam size for these maps is $20'' \times 19''$. A "medium-resolution" naturally weighted image cube was constructed from the same dataset and has a beam size of $33'' \times 33''$. This map gives a higher signal-to-noise ratio on extended, low brightness H I. A third "low-resolution" cube, used for tracing the faintest, most extended emission, was constructed from the D configuration data only using a 4 kλ taper. The beam size of this cube is $64'' \times 62''$. At the assumed distance of 5 Mpc, the angular scale of Maffei 2 is 24.2 pc arcsec^{-1}, yielding equivalent beam sizes of 0.5, 0.8, and 1.5 kpc for the high-, medium-, and low-resolution maps, respectively. The rms noise levels in the individual channel maps are measured to be $\sim$1.0 mJy beam^{-1}, corresponding to respective noise levels of 1.7, 0.5, and 0.2 K.

2.1. *Confusion with Galactic* H I

Data reduction for Maffei 2 is complicated by its location behind the plane of the Milky Way. Extragalactic H I observations are generally not affected by intervening Galactic H I but Maffei 2's unfortunate systemic velocity of $V_{LSR} = -20 \pm 1$ km s^{-1} (see § 5.1; correction for heliocentric velocity is negligible) results in a 100 km s^{-1} wide band of foreground H I confusion near the middle of its spectrum. The Galactic H I contamination confuses the central channel maps and necessitates careful processing to obtain reliable integrated maps and spectra.

The strong nuclear continuum source in Maffei 2 can be used to deduce the optical depth and spin temperature of Galactic H I along the line of sight. The absorption profile shown in Figure 1*a* (*filled diamonds*) shows the intensity of the nuclear peak as a function of velocity in the high-resolution image cube. The nuclear source shows significant absorption across seven channels (72 km s^{-1}). If the emission profile for the foreground H I is known, it is possible to apply a simple single-component radiative transfer model from which we may determine the foreground optical depths and spin temperatures.

We obtained the H I emission profile from the Berkeley Low Latitude Survey of H I (Weaver & Williams 1974) for the position ($l = 136°30'$, $b = -0°15'$). This spectrum, boxcar smoothed to a velocity resolution of 10 km s^{-1} to match our H I observations, is presented in Figure 1*b* (*filled diamonds*). The Berkeley survey was conducted with the (late) Hat Creek 85 foot (26 m) telescope, which had a beam size of 35'.5, comparable to the VLA primary beam. We have corrected the survey brightness temperatures for the telescope efficiency of 0.85 (Weaver & Williams 1973). The Berkeley survey shows the Galactic emission profile to be slowly varying across scales of $\sim 1°$. In general, H I spectra at low latitudes are uniform down to size scales of a few arcminutes due to severe blending (Bania & Lockman 1984).

We employ a single-component foreground H I radiative transfer model of the form:

$$T_{obs}(v) = T_{peak}\, e^{-\tau(v)} + T_{gal}(v)$$
$$= T_{peak}\, e^{-\tau(v)} + T_s(v)(1 - e^{-\tau(v)}),$$

where $T_{obs}(v)$ is the observed continuum absorption profile (as a function of velocity), T_{peak} is the peak nuclear continuum brightness at 21 cm of 196 K, $\tau(v)$ is the optical depth of the foreground Galactic H I, $T_{gal}(v)$ is the observed H I emission profile of Weaver & Williams (1974), and $T_s(v)$ is the spin temperature of the foreground H I. From our knowledge of $T_{obs}(v)$ and $T_{gal}(v)$ we may solve explicitly for both the foreground H I optical depths $\tau(v)$ (Fig. 1*a*; *open circles*) and spin temperatures $T_s(v)$ (Fig. 1*b*, pluses). Averaging the spin temperatures over the seven channels with the greatest signal-to-noise ratio in both emission and absorption (0 to -61 km s^{-1}) we find the mean $T_s = 90 \pm 8$ K. The emission profile inferred from this average T_s and the calculated $\tau(v)$ of the form $T_s\,[1 - e^{-\tau(v)}]$ (Fig. 1*b*, *open diamonds*) closely matches the observed profile (Fig. 1*b*, *filled diamonds*), indicating the foreground Galactic H I can be modeled reasonably by a single component of gas of uniform temperature. There is no evidence for a separate component of internal absorption against the nucleus from within Maffei 2, which, like many spirals, appears to have an H I-deficient nucleus (see § 4.1).

The presence of foreground Galactic H I compromises the quality of the data within the affected $\sim$70 km s^{-1} velocity range. Even if our single-component foreground H I model were completely accurate, indicating a uniform slab of gas with no structure on even arcminute scales, optical depths of ≥ 1 in four channels would make it difficult to recover accurate fluxes. In practice, the situation is rather more difficult as the foreground emission is probably not uniform across the $\sim 10'$ extent of H I in Maffei 2.

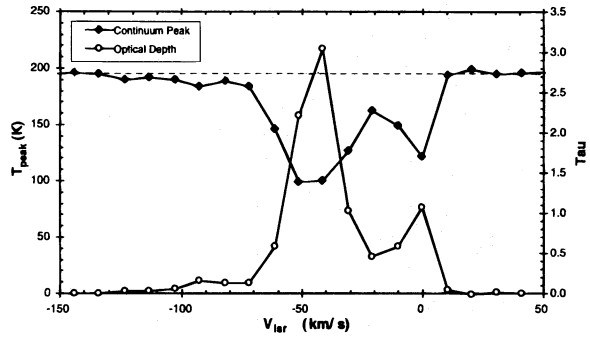

FIG. 1*a*

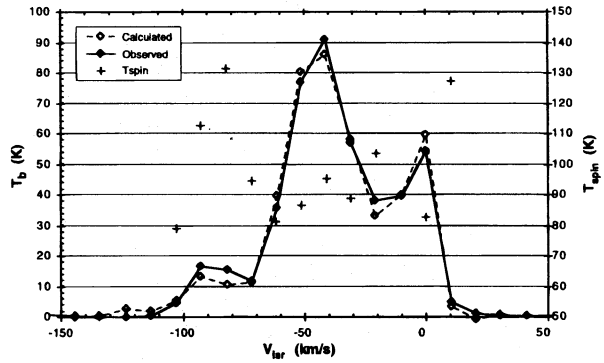

FIG. 1*b*

FIG. 1.—Continuum absorption in Maffei 2 and Galactic H I emission. (*a*) The absorption due to Galactic H I is seen in the peak continuum fluxes in the CLEANed, uniformly weighted channel maps. At positive velocities, the peak flux of the continuum emission is constant at an average value of 0.126 Jy beam^{-1}. Continuum absorption is sharply evident from $v \sim -61.8$–0.1 km s^{-1}. At lower velocities, the amplitude of the continuum peak varies irregularly. (*b*) The profile for Galactic H I emission in the direction of Maffei 2 ($l = 136°$, $b = 0°.5$; Weaver & Williams 1974) is shown with the line profile for the optical depths inferred from the continuum absorption profile. H I spin temperatures are assumed to be constant across the line.

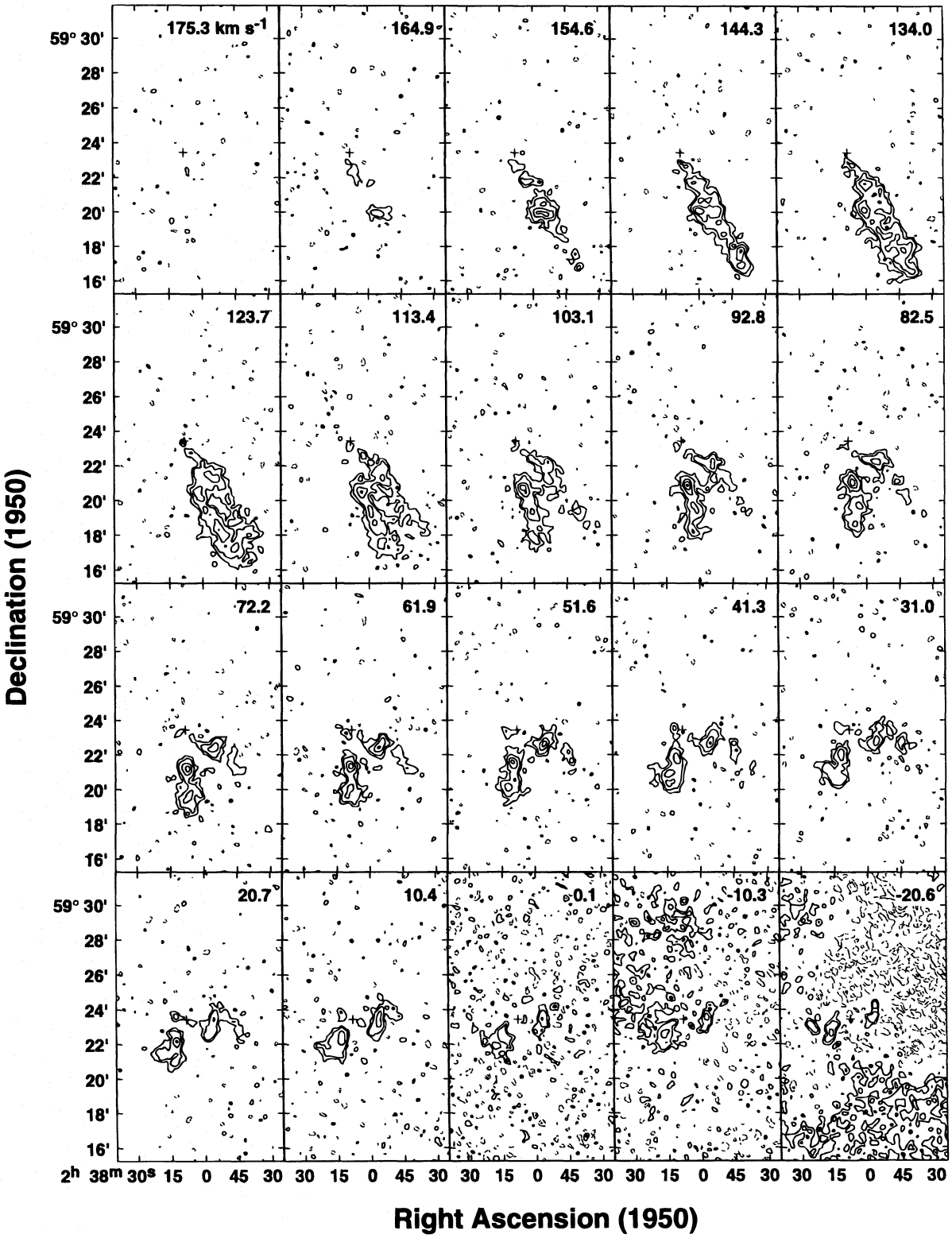

FIG. 2.—Uniformly weighted H I channel maps. These channel maps show the full range of H I emission detected in Maffei 2. The restored FWHM of the beam is 20″ × 19″, and the velocity resolution is 10.3 km s^{-1}. Contour levels are ±3, ±6, ±12, 18, and 24 mJy beam^{-1} (corresponding to ±4.7, ±9.3, ±18.7, 28.0, and 37.3 K) with the lowest contour equivalent to ~3 σ in the unconfused channels. The effects of Galactic confusion are evident in the −92.7 to +0.1 km s^{-1} channels.

Therefore applying this model naively to the dimmer line emission in the disk to reconstruct the actual emission profiles could lead to systematic errors.

A more significant effect than the foreground absorption, however, is artifacting in the maps caused by the highly extended foreground H I *emission*. The irregular spatial sampling of an interferometer limits its ability to reconstruct emission across large angular scales. While the shortest spacings in the D configuration data are sensitive to structures extending across about half the primary beam,

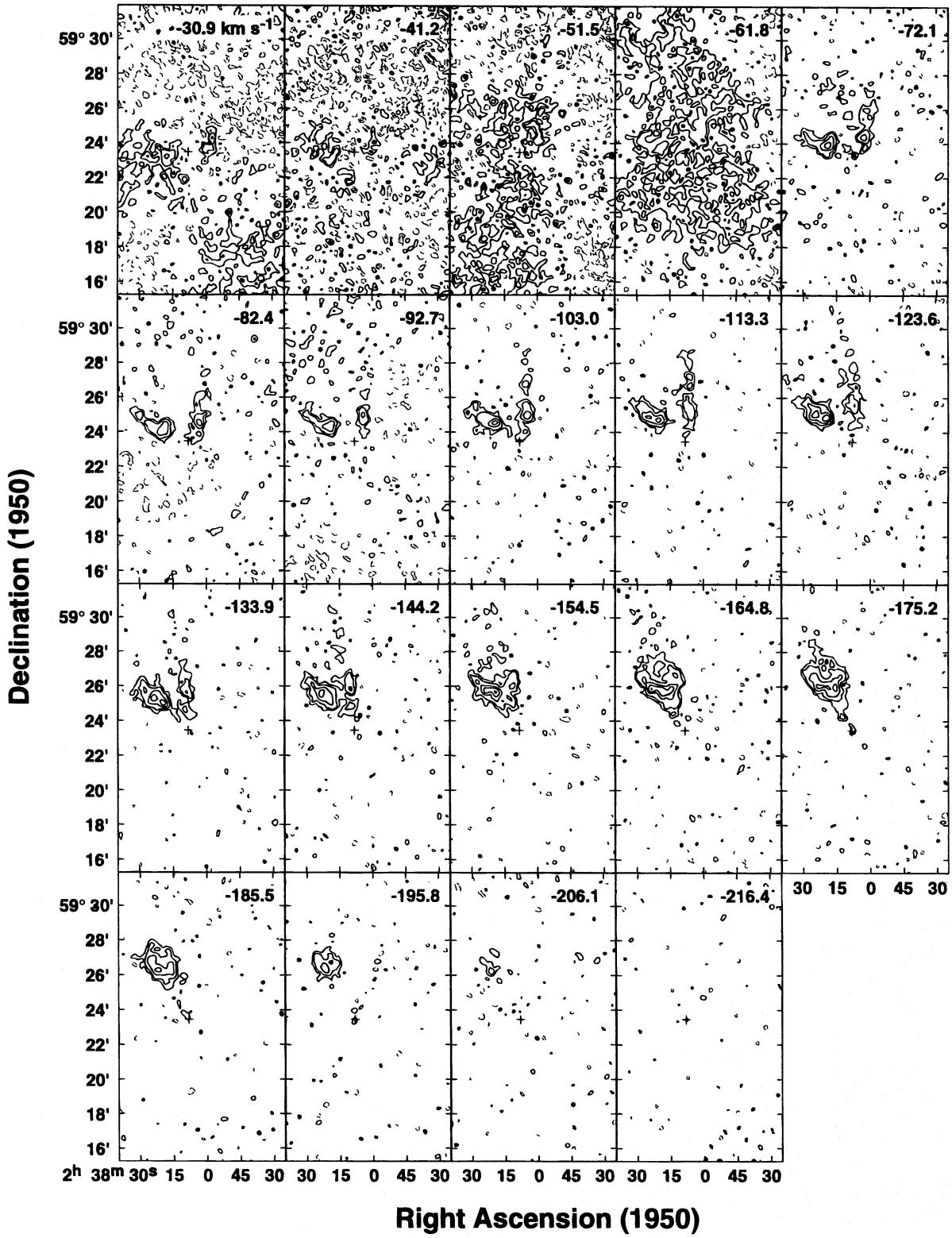

FIG. 2—*Continued*

they lack sufficient sampling to reconstruct the large-scale foreground emission reliably. The deleterious impact of undersampled foreground H I emission is less serious in the high-resolution images that are not as sensitive to weak, large-scale structure but becomes increasingly significant in the lower resolution images that weight the shorter spacings more heavily. Because of this, we made no attempt to CLEAN or otherwise deal with the confused channels in the low-resolution maps (§ 4.2).

In the following sections we outline the methods we have employed to partially compensate for confusion in the affected channels. Our goal is to extract information on the *overall* morphology and velocity structure in the galaxy, and not to make detailed analysis of the subtleties of the gas

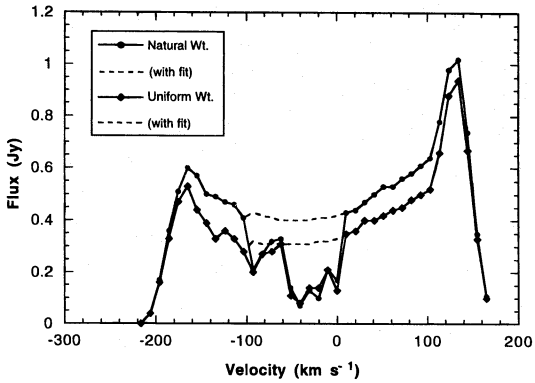

FIG. 3.—H I spectra. The total integrated H I spectra are shown for both the naturally and uniformly weighted blanked channel maps. In the channels unaffected by Galactic absorption, the uniform maps contain 84% of the integrated flux of the natural maps. The dashed lines indicate the best quadratic fits of the H I emission at the velocities affected by Galactic absorption.

in these channels. Fortunately, the bulk of H I emission in Maffei 2 lies outside the region of Galactic confusion and does not require any unusual reduction techniques.

2.2. *Channel & Moment Maps*

The high-resolution channel maps were constructed by subtracting a mean continuum image from the "dirty" line plus continuum maps. The continuum image was made by averaging the channels in the ranges $V_{LSR} = 309.2$ to 175.2 and -216.4 to -298.9 km s^{-1}; it was subtracted from the channel maps to isolate the line emission (there is some hint of faint emission in the 175.2 and -216.4 km s^{-1} low-resolution channels which did not appear at the 2 σ level in the high-resolution maps and should not affect the quality of this continuum map). In the channels strongly affected by Galactic absorption, the subtracted Maffei 2 continuum map was scaled down uniformly in intensity so that its peak matched the absorption of the peak seen in each channel (Fig. 1*a*). This was done to prevent continuum over-subtraction in these channels affected by Galactic H I so that weaker traces of line emission were not lost near the center of the galaxy. Subtracting the full continuum map would leave a negative absorption feature near the nucleus strong enough to obscure any residual line emission here. The continuum and channel maps were then CLEANed.

The resulting uniformly weighted, high-resolution channel maps are shown in Figure 2. Galactic H I contamination appears in the -92.7 to 0.1 km s^{-1} channels. The prominent rifts and ridges in the absorbed channels are artifacts of undersampling. In spite of Galactic contamination, the basic morphological features of the H I emission from Maffei 2 are visible in these maps (and there are no obvious artifacts resulting from our subtraction of appropriately scaled-down continuum emission). The lowest contour in the channel maps, which is at the 3 σ level in the uncontaminated channels, is equivalent to a column density of $N_{HI} = 8.8 \times 10^{19}$ cm^{-2}.

The substantial effects of Galactic confusion in 10 of the channel maps necessitated careful blanking techniques to preserve the information on the spatial distribution of H I in them. This information is critical for producing a proper velocity moment map and representative rotation curve. Fortunately, even in the worst high-resolution channel maps the general location of the H I peaks are evident.

Our approach was to blank all the background emission that was not correlated between channels. Inspection of the clear channels showed typical H I line widths to be $\gtrsim 30$ km s^{-1} ($\gtrsim 3$ channels) in the disk of Maffei 2, indicating that channel-to-channel correlations would help identify true emission features in the confused channels. The data cubes were inspected in velocity-declination space, and regions outside the obvious correlated emission were manually blanked. The resulting blanked maps were then convolved to larger beams (40″ for uniform weighting and 60″ for natural weighting) to smooth over the jagged variations across R.A. and then used as "cookie-cutter" templates for flux-limited blanking of the original maps. This process included all obvious emission from the clear channels and the emission peaks from the confused channels.

The H I spectra for both high (20″ beam) and medium (33″ beam) resolution maps (Fig. 3) were made by summing the fluxes across the blanked channels. Channels affected by Galactic confusion are readily recognized for their uneven, reduced fluxes. The minimum detected H I flux (excluding the corrupted channels) from the more sensitive medium-resolution maps is $S_{HI} > 142$ Jy km s^{-1}, corresponding to an H I mass of $M_{HI} > 8.4 \times 10^8\ M_\odot$ at the adopted distance of 5 Mpc. The corresponding high-resolution spectrum possesses only 83% of the flux seen in the low-resolution spectrum, presumably due to reduced weighting on the shorter spacings in the uniformly weighted maps. To improve estimates of the total H I flux and mass we interpolated over the confused part of the spectra with quadratic fits to the "bowl" of the spectrum (Fig. 3; *dashed lines*). This increased the H I flux from the high-resolution map to $S_{HI} = 185$ Jy km s^{-1}, or $M_{HI} = 1.1 \times 10^9\ M_\odot$. This value is consistent with the previously published interferometric values of $7.8 \times 10^8\ M_\odot$ (Shostak & Weliachew 1971) and $9 \times 10^8\ M_\odot$ (Wright & Seielstad 1973); it also represents 80% of the $1.4 \times 10^9\ M_\odot$ derived from the single-dish observations (Bottinelli et al. 1971). All observations have been scaled to 5 Mpc and adjusted for Galactic confusion by the respective authors in various ways.

3. RADIO CONTINUUM MORPHOLOGY

Radio continuum emission is known to trace spiral arms in galaxies. Predominantly nonthermal, it is often associated with H II regions and dust lanes in both spiral arms and bars (e.g., M83, Ondrechen 1985; M51, Mathewson, van der Kruit, & Brouw 1972; Tilanus et al. 1988; NGC 1097, Ondrechen, van der Hulst, & Hummel 1989). An independent radio tracer of spiral morphology is welcome in Maffei 2, where the high foreground extinction ($A_V \sim 5$ mag; Spinrad et al. 1973) had for many years precluded unambiguous determinations of the galaxy's stellar morphology. Recent near-infrared observations, suffering from only ~ 0.5 mag of extinction, have revealed a markedly disturbed bar and uneven spiral arms suggesting a Hubble type of SBb(s) pec (Hurt et al. 1993a).

The 20 cm continuum image of Maffei 2 (Fig. 4*a*) exhibits evidence for a well-defined nucleus, a bar running NE to SW, spiral arms of different lengths, and a diffuse disk. Our map is similar to the Westerbork map of Allen & Raimond (1972), although we are better able to resolve spiral features with our 20″ resolution. In Figure 4*b* the radio continuum image (*contours*) is compared to the near-infrared H band image (gray scale) of Hurt et al. (1993a). It is striking that all of the continuum features discussed in the following para-

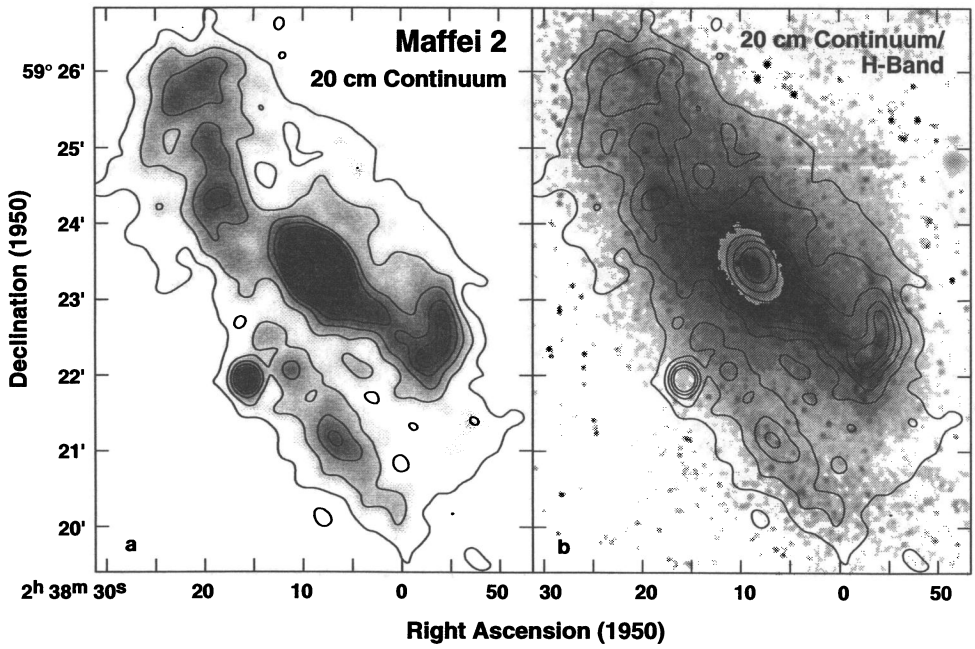

FIG. 4.—21 cm continuum emission. (*a*) The radio continuum emission in Maffei 2 is shown in contour and gray scale. (*b*) The continuum emission contours are overlaid on an H-band image of the galaxy (Hurt et al. 1993a). Contour intervals in both figures are at 1.5, 3, 4.5, 6, 7.5, 15, 30, 60, and 120 mJy beam^{-1} for a 20.″2 × 19.″1 beam. The lowest contour corresponds to 5 σ and the peak is at 130 mJy beam^{-1}. Alignment of the maps is better than 5″. The bright stars have been subtracted from the H-band image to increase clarity of the extended features. The inner ncuelus is displayed in a different stretch to bring out saturated details.

graphs have clear analogs in the H band, which traces the base stellar disk. Such a close correspondence alleviates any concerns that the disturbed appearance in the near-infrared might be caused by foreground Galactic extinction effects.

The nuclear starburst is the strongest radio continuum source in Maffei 2. The starburst has an infrared luminosity of $4 \times 10^9\ L_\odot$ (Rickard & Harvey 1983, 1984), similar to that of the starburst in M83. The peak radio flux density in the nucleus is $S_{1.4\ \mathrm{GHz}} = 130 \pm 10$ mJy beam^{-1} from a 10″ × 20″ source (deconvolved FWHM, assuming a Gaussian structure). This is similar to the 8″ × 15″ knotty ridge of bright 6 cm continuum emission running north-south through the nucleus (Seaquist, Pfund, & Bignell 1976; Turner & Ho 1994). The total flux for the nucleus is 230 ± 10 mJy, consistent with the Westerbork value of 210 ± 10 mJy (Allen & Raimond 1972). Combining this with the VLA mapped 2 and 6 cm fluxes of 46 and 107 mJy (Turner & Ho 1994) we find an overall spectral index of $\alpha = -0.7$ for the nucleus ($S_\nu \sim \nu^\alpha$) indicating the nuclear emission is dominated by nonthermal synchrotron emission. The radio emission is spatially well-correlated with intense mid-infrared emission (Ho et al. 1989; Telesco, Dressel, & Wolstencroft 1993). The nuclear continuum emission at 21 cm is probably caused by a population of young supernova remnants directly associated with the starburst.

To the west and south of the bright nucleus, a barlike feature can be traced from the nucleus to a radius of ~2′. This bar connects smoothly to a spiral arm that extends to the west and north. This radio continuum ridge closely follows the corresponding H-band spiral arm (Fig. 4*b*), although the radio centroid may be displaced slightly toward the dust lane. This is like the situation in M51, where the nonthermal continuum arms also appears to be closely associated with the dust lanes in the spiral arms while the less abundant thermal emission lies within the stellar arms (Tilanus & Allen 1988). While the continuum in Maffei 2 is not centered on the dust lanes as is seen in M51, beam smearing effects along sharp-edged distributions, as discussed by Tilanus et al. (1991), will tend to displace unresolved emission more toward the spiral arm than the dust lane. The enhanced continuum emission in the arms is probably caused by either enhanced magnetic fields or increased cosmic-ray densities in the compression/shock region of the spiral density wave (see, e.g., Mathewson et al. 1972; Tilanus et al. 1988).

The radio continuum emission to the north and east of the nucleus in Maffei 2 is more complex than it is in the southwest bar and arm. The northeastern segment of the bar has reduced intensity and broader width than its southwestern counterpart. The northeast bar connects to a broken ridge of emission that both leads and trails the end of the bar. Hurt et al. (1993a), who first reported this "leading" spiral arm feature in the near-infrared, have suggested it is a tidal arc associated with an interaction with a small companion galaxy, which can be seen as a low brightness condensation to the north. The location of this potential companion coincides with the northernmost peak of continuum emission, centered at $\alpha = 2^h38^m21^s.5$, $\delta = 59°25'.8$, with a total flux of $S_{1.4\ \mathrm{GHz}} = 17 \pm 2$ mJy. A ridge of emission connects this object to the northeast end of the bar. Such an extension is reminiscent of other radio continuum arcs found between interacting pairs like M51/NGC 5195 (Mathesson et al. 1972; Tilanus et al. 1988) and NGC 3395/NGC 3396 (Huang et al. 1994). The trailing spiral arm extending south of the northern bar end is a broken ridge ~4′ in length, much longer than its counterpart western arm. Such asymmetries are classic signatures of tidal interactions, an issue that is addressed further in § 6.1.

A prominent, unresolved continuum peak lies ~2′ to the southeast of the nucleus. Although its proximity to the spiral arm suggests an association with Maffei 2, it appears

to be a background active galaxy. Its flux of $S_{1.4\ \mathrm{GHz}} = 12 \pm 1$ mJy beam^{-1} shows no decline from the map of Allen & Raimond (1972), whose observations predate ours by about 14 yr; a recent radio supernova would likely exhibit an observable decline (Weiler et al. 1986). It is also seen at 6 cm (Turner & Ho 1994), where it is resolved into a double-lobed source with a spectral index of $\alpha = 1.0$—characteristics typical of background active galaxies.

In addition to the bar and spiral features, we find a nearly uniform halo of emission in the disk of Maffei 2. Its extent closely mimics the observed stellar disk (Fig. 4*b*). The mean intensity of this halo is 3.4 ± 0.5 K (2.2 ± 0.3 mJy beam^{-1}).

4. H I MORPHOLOGY

4.1. *High-Resolution Maps: The Detailed Structure*

The high-resolution H I integrated intensity maps are presented in Figure 5. These are constructed from the high-resolution channel maps described in § 2.2. To partially compensate for foreground H I confusion we scaled up the affected channels to match the interpolated H I fluxes in these channels (§ 2.2). This rescaling has been applied to minimize nonphysical artifacts in the integrated moment maps caused by the sharply reduced fluxes in the recovered emission (see Fig. 3). The spatial regions correlated with the foreground H I confusion must nonetheless be interpreted with care; dashed lines indicate the southern and northern edges of emission in the 10.4 and -82.4 km s^{-1} channels, respectively, delineating the largest possible region suffering from confusion effects. The H I morphology and velocity field match smoothly both inside and outside this region, implying that our interpolation has introduced no physically unreasonable artifacts. The greatest possible uncertainties in this region are in flux and morphology; the velocity field should be reasonably accurate since it is primarily dependent on the spatial centroids of emission which are recovered in the channel maps despite confusion.

The H I in Maffei 2 lies predominantly in a circumnuclear "ring," with little or no emission in the nucleus (Fig. 5*a*). Although the nucleus does lie within the regions affected by Galactic confusion, the absence of significant H I here is not a confusion effect. Molecular gas in the inner 1′ of the nucleus exhibits a broad emission profile, spanning $V_{\mathrm{LSR}} = -145$ to 100 km s^{-1} (Hurt & Turner 1991). If a substantial amount of nuclear H I were present, it would be clearly evident in the $V_{\mathrm{LSR}} = -134$ to -103 and 10 to 144 km s^{-1} channel maps (Fig. 2). Neither is there evidence for self-absorption that might mask H I emission (§ 2.1). H I holes in the nuclei of spiral galaxies are known to be relatively common (see, e.g., Wright 1974; Giovanelli & Haynes 1988).

The H I "ring" in the disk of Maffei 2 actually consists of two arms encircling the nucleus, which correspond well with, but extend beyond, the 20 cm continuum (Fig. 5*b*) and near-infrared emission. The overall H I emission extends well beyond the radio continuum and near-infrared disk along the general directions of the observed spiral arms, as is seen in other barred galaxies (e.g., NGC 1097, Ondrechen et al. 1989; NGC 1300, England 1989; NGC 1365; Ondrechen & van der Hulst 1989; NGC 4731; Gottesman et al. 1984).

The H I distribution in Maffei 2 is markedly asymmetric. The northern part of the H I disk extends roughly half the distance of the southern disk. While the western arm can be traced only about 4′ north of its bar end (this is possibly an

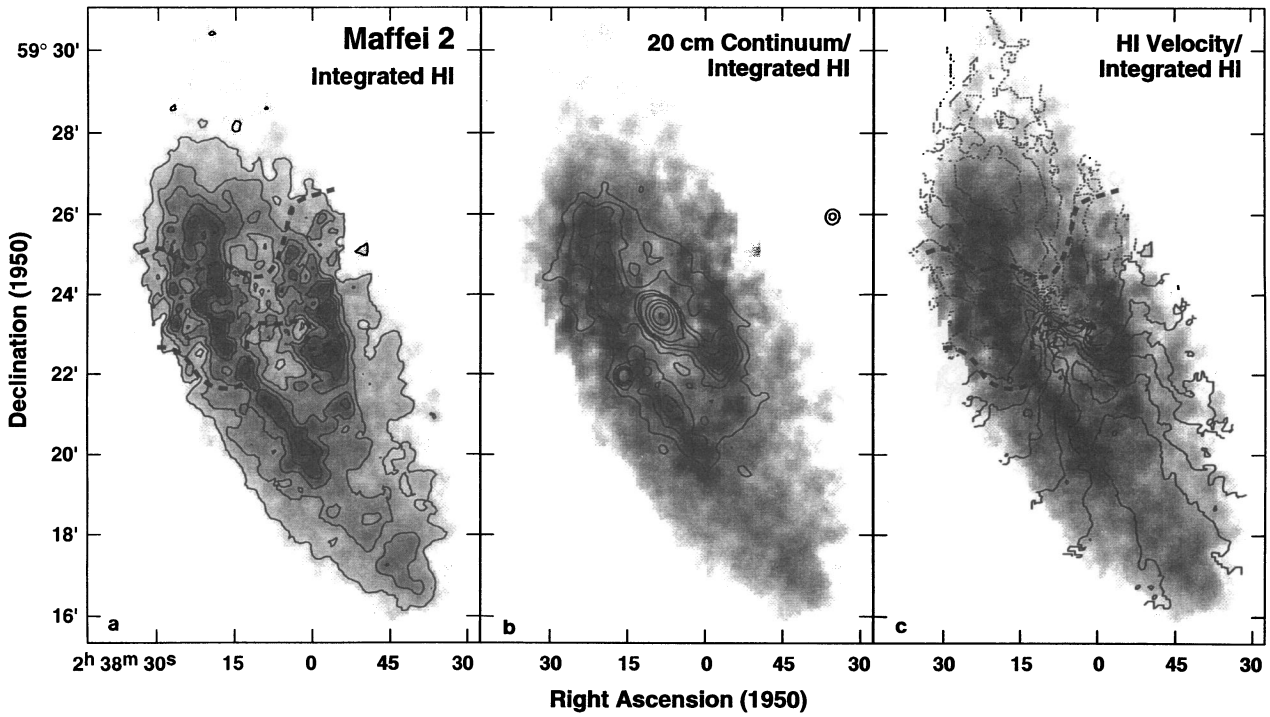

FIG. 5.—Integrated H I emission and velocity field. (*a*) The integrated H I emission $\int I(v)dv$ is shown in gray scale and contours. The contour levels are at 0.1, 0.3, 0.5, 0.7, 0.9, 1.1, and 1.3 Jy beam^{-1} km s^{-1} (corresponding to 1.6, 4.7, 7.8, etc., $\times 10^2$ K km s^{-1} or column densities of 2.8, 8.5, 14.2, etc., $\times 10^{20}$ cm^{-2}. (*b*) The 21 cm continuum emission (*contours*) is overlaid on the integrated H I emission (gray scale). Contour levels are as in Fig. 4. (*c*) The mean intensity weighted H I velocity field $[\int vI(v)dv]/[\int I(v)dv]$ (contour) is overlaid on the integrated H I emission (gray scale). Contours range from -175 to 125 km s^{-1} at 25 km s^{-1} intervals. Negative contours are dashed. In both (*a*) and (*c*), the bold dashed lines indicate the full extent of H I emission in the 10 channels that are most affected by Galactic extinction; any detailed structure or emission intensities in this region are suspect.

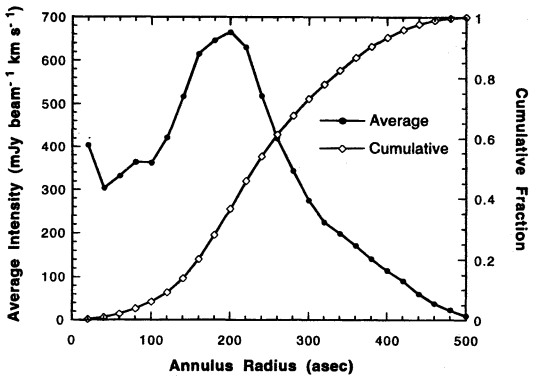

FIG. 6.—Azimuthally averaged radial H I profile. The azimuthally averaged integrated H I intensity is plotted by the line with filled circles. The H I clearly peaks at a radius of 200″ (5 kpc). The cumulative flux contained within the radius R is plotted with open diamonds.

overestimate due to the rescaled confused channels; the continuum extent is much shorter), the eastern arm extends nearly 8′ (12 kpc) south of its bar end (the entire eastern ridge, including the northern extension, extends over 10′ (14 kpc). Analogous asymmetries in the spiral arms have been observed in near-infrared observations (Hurt et al. 1993a). The northern H I arm actually breaks into a "double-arc" structure, which we discuss further in § 6.2.

The azimuthally averaged H I integrated intensity shown in Figure 6, corrected for projection, highlights the annular nature of the atomic gas. The H I surface density peaks at a radius of 200″ from the nucleus with 70% of the flux contained within a ring extending from 100″ to 300″ (2.4–7.3 kpc) in radius. The peak average intensity corresponds to a column density of $N_{\rm H} = 2 \times 10^{21}$ cm^{-2}, equivalent to an H I surface density of 16 $M_\odot$ pc^{-2}. No H I is detected beyond a radius of 9′. The relatively high average intensity of H I within a radius of 100″ is likely due to large contributions from the confused channels and cannot be trusted. However, regardless of the exact level of H I, the nucleus is clearly dominated by molecular gas, with a peak hydrogen atom column density of $N_{\rm H} \sim 3 \times 10^{22}$ cm^{-2}, as inferred from ^{13}CO observations (Hurt & Turner 1991) and averaged over a matching 20″ beam.

4.2. *Low-Resolution Maps: The Total* H I *Disk Extent*

The most obvious asymmetry in the H I distribution of Maffei 2 is the mismatched arms to the north and south. While there is a substantial quantity of H I south of the eastern spiral arm, there is little emission to the north. However, the patchy noiselike structure in the high-resolution channel maps (Fig. 2) in this region hints that there could be low-level, extended emission to the north. To investigate this possibility we used the low-resolution (1′

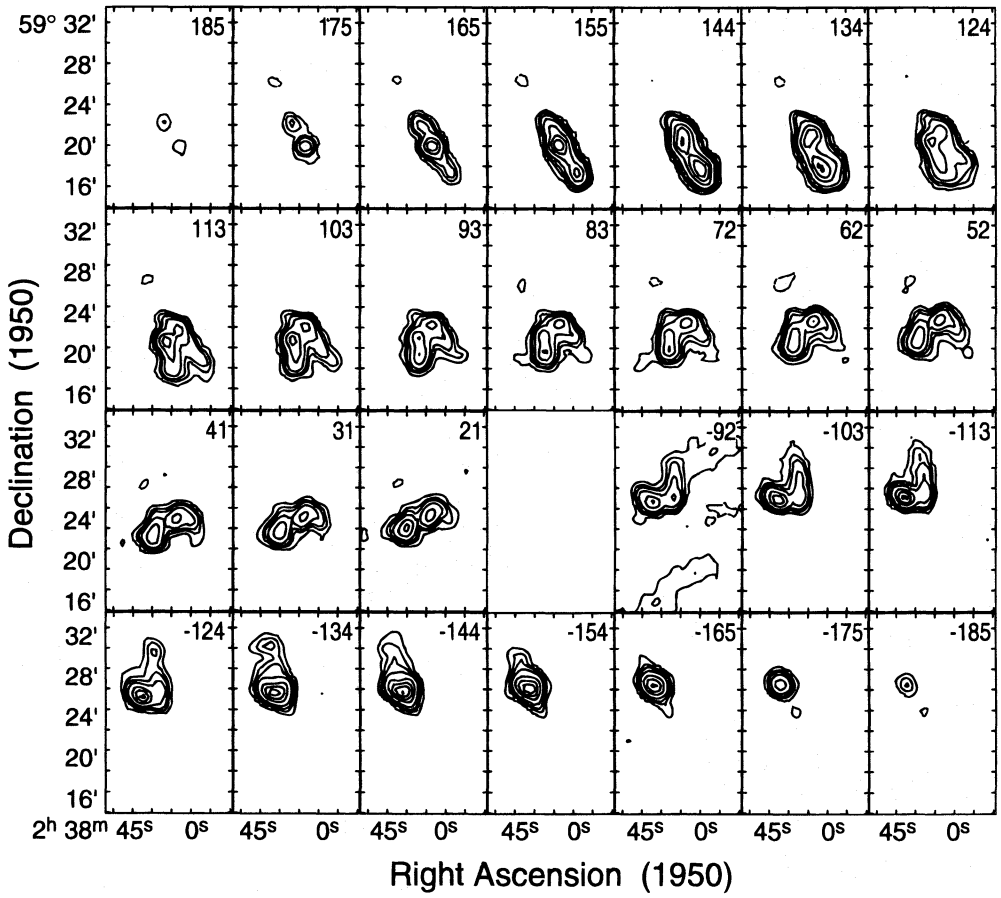

FIG. 7.—Low-resolution H I channel maps. These channel maps show the full range of H I emission detected in outer disk of Maffei 2. The beam size for these maps is 64″ × 62″, P.A. 90°. Contour levels are at ±3, ±6, ±12, 18, and 24 mJy beam^{-1} (corresponding to ±4.7, ±9.3, ±18.7, 28.0, and 37.3 K), with the lowest contour equivalent to ~2.5 σ for the clear channels. The channel maps for the −82 to 0 km s^{-1} channels are highly corrupted by Galactic absorption and are not shown.

beam) maps produced from only the D configuration data. The lowest contour of these channel maps (Fig. 7), which is at the 4 σ level of 5 mJy beam^{-1} (0.7 K), corresponds to a column density of $N_{\rm H\,I} = 1.4 \times 10^{19}$ cm^{-2}, nearly an order of magnitude lower than the high-resolution maps. The effects of confusion with Galactic H I are more pronounced in these maps (the affected channels have been omitted from the figure), but this does not interfere with the northern or southern H I reaches of the galaxy. Integrated column densities in the northern extension are $N_{\rm H\,I} \sim 1$–5×10^{19} cm^{-2}, about 1 order of magnitude lower than in the corresponding southern extension. The northern section has a peak H I surface density of $\sim 0.3\ M_\odot$ pc^{-2}.

Another difference between the northern and southern disks is a difference in position angle. The line of symmetry in the south is along the line of nodes, at P.A. 206°, as expected. However, in the north, the line of symmetry is markedly different, at P.A. ~0°. The shift in position angle appears in the -103 to -154 km s^{-1} channels, where there is a ridge of emission that runs nearly north-south. The high-intensity high-dispersion H I "bright spots" at the ends of the bar are relatively symmetric on the north and south sides. The position angle shift appears to occur in the low column density material further out in the disk. In § 6 we discuss a possible explanation for this disturbance.

5. H I KINEMATICS

5.1. *Rotation Curve and Mass Models*

We derive basic kinematic parameters for Maffei 2 by fitting a circular rotation curve to the intensity-weighted mean velocity field (Fig. 5*c*) using the GAL task in AIPS to fit to a Brandt rotation curve (Brandt & Scheer 1965). The Brandt rotation curve describes an integral series of flattened spheroidal shells and takes the analytical form:

$$V(r) = 3^{2/n} \frac{V_{\rm max}(r/R_{\rm max})}{[1 + 2(r/R_{\rm max})^n]^{3/2n}}$$

Our best fit, for $n = 0.5$, yields a maximum velocity of $V_{\rm max} = 172.0$ km s^{-1} at a radius of $R_{\rm max} = 322''$ (7.9 kpc). From these parameters we infer a total dynamical mass of $M_{\rm T} = 6.7 \times 10^{10}\ M_\odot$ for $R < 500''$ (12 kpc; the total observed extent of H I). As the Brandt curve is fitted to the entire velocity field, from it we also derive the properties of inclination $i = 67° \pm 1°$, P.A. $= 206° \pm 1°$, and systemic velocity $V_{\rm sys} = -20 \pm 1$ km s^{-1}. The values derived for these properties are insensitive to the chosen exponential factor n, depending primarily on the geometry of the velocity field. These results are summarized in Table 1.

The mean rotation curve for Maffei 2, presented in Figure 8*a* was obtained from three slices across the velocity field, one along the major axis and the other two at $\pm 10°$ offsets. After correcting for projection and for angular displacement off the major axis, the data were averaged in 20″ bins to derive the mean rotation curve (Fig. 8*a*; *circular markers*). There is excellent agreement between the northwest and southeast halves of the velocity field; the data from the two sides of the galaxy cannot be distinguished from one another in the rotation curve (Fig. 8*a*, *pluses*). This rotation curve is not valid for the nuclear regions; for small radii ($R \lesssim 100''$) the 20″ beam blends regions that sample kinematically distinct regions of the highly inclined disk, effectively tapering the curve to lower velocities.

TABLE 1

MAFFEI 2 PROPERTIES

Property	Value
Hubble Type[a]	SBb (s) pec
Distance[b]	5 ± 1 Mpc
Dynamical Center (H I):	
R.A. (1950)	$2^{\rm h}38^{\rm m}7\overset{\rm s}{.}8 \pm 0\overset{\rm s}{.}2$
Decl (1950)	59°23′30″ ± 1″
Systematic velocity (disk; H I)	-20 ± 1 km s^{-1}
Systematic velocity (nucleus; ^{13}CO)	-31 ± 2 km s^{-1}
Inclination	67° ± 1°
Position angle (receding axis)	206° ± 1°
H I line width (20% of peak)	350 km s^{-1}
Total interpolated H I flux	185 Jy km s^{-1}
Peak H I column density	3×10^{21} cm^{-2}
Total interpolated H I mass	$1.1 \times 10^9\ M_\odot$
Total dynamical Mass, $R < 12$ kpc (500″)	
Brandt curve	$6.7 \times 10^{10}\ M_\odot$
Spherical halo only	$8.3 \times 10^{10}\ M_\odot$
Exponential disk + halo	$5.4 \times 10^{10}\ M_\odot$

[a] Hurt et al. 1993b.
[b] Spinrad et al. 1973.

An independent check of the rotation curve is provided in the form of a position-velocity (PV) diagram taken along the major axis of the galaxy (Fig. 9). The horizontal and vertical dashed lines indicate the systemic velocity and dynamical center, respectively. A PV rotation curve may be

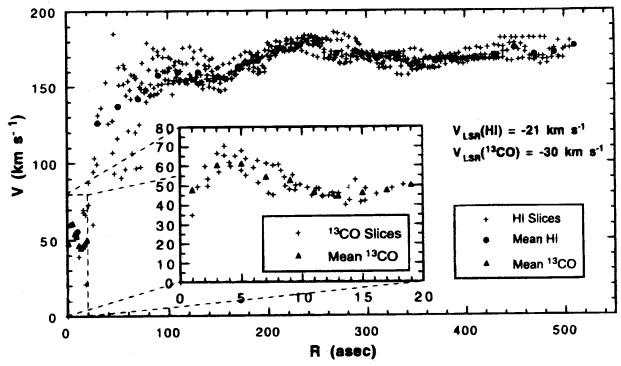

FIG. 8*a*

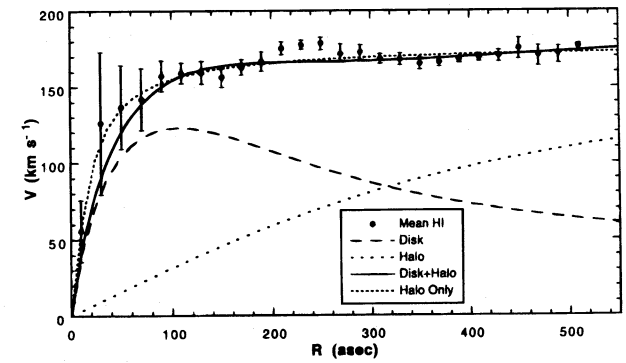

FIG. 8*b*

FIG. 8.—H I rotation curve. (*a*) Pluses mark data points taken from a slice through the major axis and from slices 10° to either side of it. Filled circles mark the binned average values from this data. The inset shows the inner rotation curve determined from ^{13}CO observations (Hurt & Turner 1991); filled triangles indicate averages on both the inset and main chart. (*b*) The average rotation curve is shown with two different fits for the mass distribution (see § 6.4.1). Error bars indicate 1 σ uncertainties for the averages.

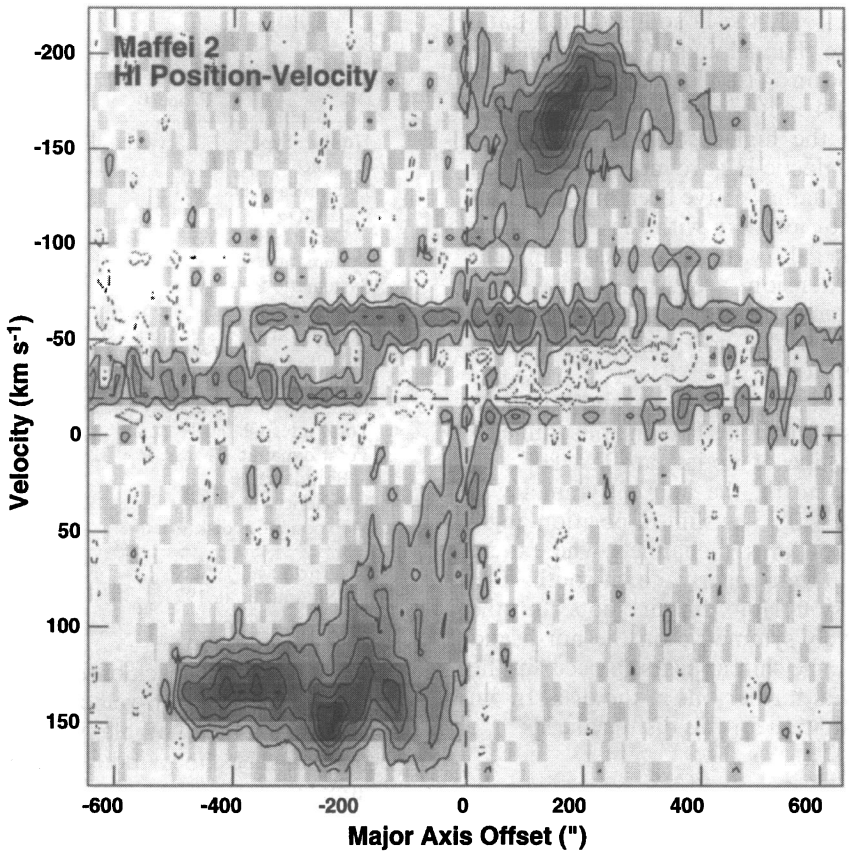

FIG. 9.—Major axis position-velocity cut. This position-velocity (PV) diagram was produced by averaging a 30″ wide strip through the high-resolution data cube along the galaxy's major axis. The horizontal and vertical dashed lines indicate the systemic velocity and dynamical center, respectively. Contour levels are at ±1.25, ±3, 6, 9, 12, 15, and 18 mJy beam^{-1} (corresponding to ±1.9, ±4.7, 9.3, 14.0, 18.7, 23.3, and 28.0 K). This PV diagram was prepared from the unblanked data cube; effects of Galactic confusion may be seen as horizontal stripes. The velocity axis reflects observed velocities and has not been corrected for inclination.

inferred by tracing along the peak ridge of emission, ignoring the lower velocity gas seen at inner radii. After correcting for inclination, the PV rotation curve is essentially identical to that in Figure 8 for radii $R \gtrsim 100''$. Inside this radius there is evidence for an inner velocity peak at $R \sim 50''$ although this feature is difficult to interpret because of the paucity of nuclear H I. We adopt the rotation curve derived from the velocity field for further analysis.

To better examine the mass distribution in Maffei 2 we fitted the rotation curve to a simple model that incorporates both a planar exponential disk and a spherical halo. The disk surface density σ_d and halo density ρ_h take the forms:

$$\sigma_d(r) = \sigma_0 e^{-r/R_d}, \quad \rho_h(r) = \frac{\rho_0}{1 + (r/R_h)^2}.$$

The first equation is that of a simple exponential flat disk with central surface density σ_0 and length scale R_d; the second is a halo model used for the Milky Way (Bahcall & Soneira 1980) with central density ρ_0 and core radius R_h.

A family of nonunique solutions with varying disk contributions can be found to fit the observed rotation curve of Maffei 2. A reasonable fit may be found for a purely spherical halo model with parameters $\rho_0 = 3.6\ M_\odot\ \mathrm{pc}^{-3}$, $R_h = 400$ pc. This implies a total dynamical mass for $r < 500''$ (12 kpc) of $M_h = 8.3 \times 10^{10}\ M_\odot$, equivalent to the galaxy's Keplerian mass.

Flattened mass distributions including exponential disks are more realistic for spiral galaxies and support rotation curves with less mass than is required by spherical distributions. Using the near-infrared observations of Hurt et al. (1993a), we find that the light in Maffei 2 does not follow a precise exponential disk but is more sharply peaked in the nucleus. From the range of observed scale lengths ($R_d \sim$ 2000–2800 pc) we adopt $R_d = 2400$ pc (100″). Fixing this parameter we then vary σ_0, ρ_0, and R_h to find acceptable rotation curves, biasing the fit to the most massive disk that can fit the data. For $\sigma_0 = 600\ M_\odot\ \mathrm{pc}^{-2}$ and halo parameters $\rho_0 = 10^{-2}\ M_\odot\ \mathrm{pc}^{-3}$, $R_h = 8000$ pc we obtain the fit illustrated in Figure 8*b* (*solid and dashed lines*) with masses ($r < 12$ kpc) of $M_d = 2.1 \times 10^{10}\ M_\odot$ and $M_h = 3.3 \times 10^{10}\ M_\odot$ for a total mass of $M_T = 5.4 \times 10^{10}\ M_\odot$. We found no acceptable fits for proportionally more massive disks ($M_d/M_T > 0.5$) even when the disk scale length R_d was varied.

The extreme limits of halo-dominated and disk-dominated mass models, while only endpoints in a continuum of acceptable fits, do set effective upper and lower limits on the dynamical mass of a galaxy. Overall we find the total dynamical mass of Maffei 2 to be in the range 5–8 $\times 10^{10}\ M_\odot$ within a radius of 12 kpc. Given the observed H I mass of $M_{\mathrm{H\,I}} = 1.1 \times 10^9\ M_\odot$ we find that the neutral atomic hydrogen constitutes 1%–2% of the galaxy's total mass for $R \leq 12$ kpc (500″). This ratio is somewhat

higher at smaller radii where the dynamical mass is less dominated by the extended halo [i.e., $M_{\rm H\,I}/M_T \sim 3\%$ for $R < 6$ kpc (250″)]. The observed mass ratio is in agreement with the results of Wright & Seielstad (1973) and is well within the observed range for spiral galaxies (see, e.g., Giovanelli & Haynes 1988).

In the outer parts of Maffei 2, the H I shows a clear increase in the average rotational speed peaking at $r = 5.8$ kpc (240″). This feature covers an annulus that is about 2.4 kpc (100″) wide and is not explained by our simple halo/disk models. However, the peak radial H I density (Fig. 6), tracing the stellar and gaseous spiral arms, is located just inside this radius at ~4.8 kpc (200″). The ~15 km s^{-1} rise in velocity is likely a gaseous response to locally increased disk density (from both stars and gas) in the spiral arms.

5.2. *Disk* H I *and Nuclear* CO *Kinematics*

The H I rotation curve presented in Figure 8 is valid for the outer disk of Maffei 2 but does not represent the nucleus very well. The kinematics in the inner arcminute of Maffei 2, however, has been studied at much higher resolution (6″) in the ^{13}CO (1–0) transition (Hurt & Turner 1991) and also in CO (3–2) (Hurt et al. 1993b). Here we present a rotation curve derived from the ^{13}CO data set, pushed to ~3″ resolution using maximum entropy deconvolution techniques. The ^{13}CO (1–0) rotation curve (Fig. 8*a*, *inset*) is computed from velocities measured along the observed nuclear molecular ridge that is coincidentlly aligned within ~10° of the major axis of the galaxy. Velocities were sampled from the intensity-weighted velocity moment map at ~1″ spacings along the ridge. Assuming pure circular rotation, these velocities were corrected for offset from the major axis and inclination as was done for the H I curve. The mean velocity curve (*triangles*) was averaged in 2″ bins.

A very steep initial rise in velocity is indicated by the ^{13}CO rotation curve. It reaches its peak of 60 km s^{-1} within one 3″ beam of the nucleus, after which it drops off and follows a more gentle rise. Such a sharp rise and falloff indicates a compact nuclear component nuclear component of mass $M \lesssim 1 \times 10^8\ M_\odot$ for $R < 3''$ (70 pc). While noncircular motions occurring along this azimuthally restricted CO ridge may introduce systematic uncertainties in these assumed circular rotation velocities and inferred mass, it is clear that Maffei 2 attains a significant fraction of its outer rotation velocity (e.g., 160 km s^{-1} at a radius of 90″ [2.2 kpc]) within the inner 100 pc.

An interesting difference between the ^{13}CO and H I rotation curves is the substantial inconsistency in systematic velocities. The ^{13}CO rotation curve for the inner nucleus indicates a systemic velocity of $V_{\rm sys} = -31 \pm 2$ km s^{-1}, consistent with results determined from 20″ resolution CO (3–2) observations of the nucleus (Hurt et al. 1993b). This represents an 11 km s^{-1} discrepancy, however, with the systemic velocity of $V_{\rm sys} = -20 \pm 1$ km s^{-1} derived from the H I in the outer disk. This velocity offset appears to be a real and significant effect since each systematic velocity is very well determined by minimizing the scatter between the two branches of the rotation curve. Interestingly, although the values for the systemic velocity are discrepant, the dynamical center inferred from the ^{13}CO falls within ~2″ of that found for the H I.

The most obvious interpretation of the discrepancy in systemic velocity is that the disk and nucleus of Maffei 2 possess distinct kinematic motions. These velocity determinations are made from observations that sample disjoint parts of the velocity field: the ^{13}CO (1–0) rotation curve extends only to $R < 730$ pc (30″) while the H I rotation curve is reliable for $R > 1.9$ kpc (80″). The nucleus appears to be moving 11 km s^{-1} toward us with respect to the disk. Preliminary analysis of single-dish maps of CO (1–0) and (2–1) at 50″ and 25″ resolution, respectively, confirm this systematic offset, hinting that $V_{\rm sys}$ varies smoothly across the inner disk, stabilizing at $R > 2.4$ kpc (100″) (Hurt, Turner, & Martin 1996).

5.3. *Bar Response and Corotation*

To first order, the velocity field of Maffei 2 (Fig. 5*c*) shows nonaxisymmetric motions typical of a barred galaxy. A disk undergoing pure circular rotation has isovelocity contours that are symmetric about the major axis, intersecting it perpendicularly at all points. When the inner solid body rotation crosses over to flattening differential rotation at larger galactocentric radii, the contours will bend away from the minor axis at points away from the major axis, producing the characteristic "spider" diagram. In barred galaxies, orbits are perturbed from circular symmetry toward cusped oval orbits (see, e.g. Roberts, Huntley, & van Albada 1979). The kinematic signature of such orbits is to drive the isovelocity contours to intersect the major axis at shallower angles. The S-shaped distortion in the velocity field of Maffei 2 is typical of motions in a barred potential.

Deviations from circular motion are more obvious and easier to quantify once a uniform circular velocity field has been subtracted from the observed velocity field. The residual velocity field in Maffei 2 (after subtraction of the best-fit Brandt rotation curve; § 5.1) is presented in Figure 10, smoothed to 30″ resolution to emphasize large-scale variations. The white/black scale covers a velocity range of ±25 km s^{-1} in Figure 10*a* and ±5 km s^{-1} in the higher contrast Figure 10*b*.

The sharpest discontinuity in residual velocity is across the major axis in the nucleus of the galaxy, evident as the prominent black/white bipolar feature in Figure 10. This residual velocity jump has a peak-to-peak value of ~ ±50 km s^{-1} across a deprojected distance of ~2.2 kpc (1′.5). This bipolar pattern is caused by the noncircular response to the barred potential. Farther out in the disk of Maffei 2 the steepest velocity gradients lie across the spiral arms, caused by streaming motions along the spiral arms. Indicated by the contoured H I ridges overlaid in Figure 10*a*, the arms clearly follow the gray transition regions between the velocity extrema.

In addition to the basic bipolar pattern expected for a symmetric barred galaxy, the morphological asymmetries in Maffei 2 have corresponding asymmetries in the associated velocity residual patterns. The velocity gradient in the southwest H I arm lies predominantly on the *outside* of the arm; the peak positive residual velocities lie well outside the contour and reach values of approximately +25 km s^{-1}. Along the northeast arm the velocity gradient is on the *inside* of the arm and is not as steep; the corresponding peak negative residuals lie within the contour and reach peak values of only about ~ −10 km s^{-1}. Similarly, there is a much larger overall gradient across the southwest arm, $\Delta v_{\rm res} \sim 30$ km s^{-1} (defining the arm width by the overlaid contour in Fig. 10*a*), as compared with $\Delta v_{\rm res} \sim 20$ km s^{-1} for the northeast arm, and there only at the northern tip near the bar end. The smaller velocity gradients typical of

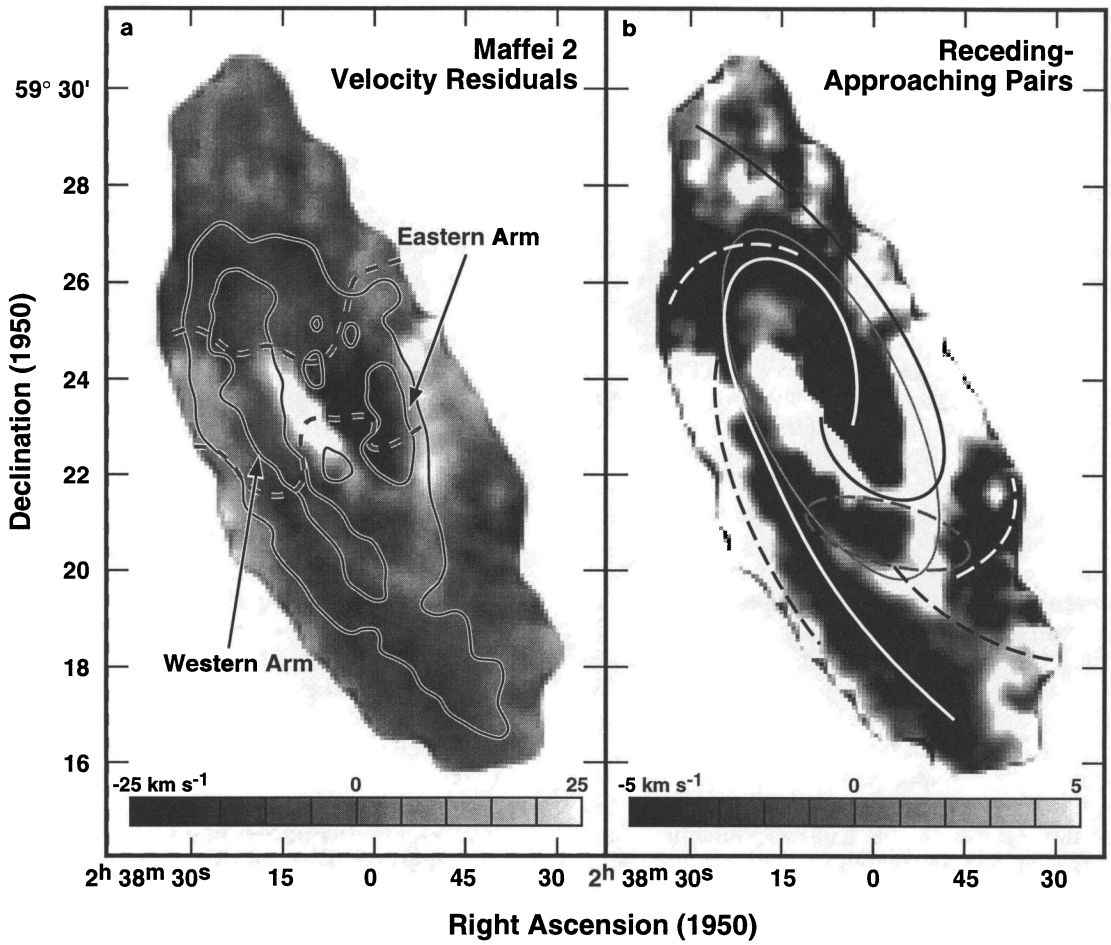

FIG. 10.—Velocity residuals. The velocity residuals rendered in a gray scale are calculated by subtracting the best Brandt circular rotation curve (§ 5.3) from the velocity field. Velocity ranges are ± 25 km s^{-1} (*a*) and ± 5 km s^{-1} (*b*). The residual maps have been smoothed slightly. Two smoothed contours of the integrated H I are overlaid in (*a*) to show the locations of the H I arms with respect to the velocity gradients. Approaching-receding pairs are traced with lines in (*b*). Solid lines indicate resonances extending from the nucleus to the disk while dashed lines indicate new pairs created at corotation. The potential corotation radius of 4′ is marked by the gray ellipse. The dashed gray ellipse indicates the largest deviations from the traced resonance arms.

the northern bar region are associated with the fuzzier, ill-defined bar/arm morphology there.

The residual velocity field can, in principle, be used to help locate dynamical resonances in Maffei 2. Canzian (1993) has demonstrated that the location of a corotation resonance can be identified by the number of approaching-receding arms seen in the velocity residual field. Inside corotation, where the particles overtake the more slowly rotating density wave, a two-armed spiral will have 2–1 = 1 approaching-receding pair while outside corotation where the density wave overtakes the particles there will be 2 + 1 = 3 pairs. There is tentative evidence for a corotation effect in the Maffei 2 velocity field. Drawn in Figure 10*b* are lines tracing possible approaching-receding pairs (*white-black lines*). The solid lines indicate a primary pair extending from the nucleus to the outer disk. The dashed lines indicate secondary pairs which appear outside corotation. The gray ellipse (*solid line*) shows a projected circle 4′ in radius positioned where the secondary resonant arms appear. These results hint at a corotation radius of ~ 5.8 kpc (4′), just outside of the traceable arms and bar in Maffei 2 (the largest deviation from this model is indicated by the dashed gray ellipse). Corotation at this radius would imply a pattern speed for the spiral arms of ~ 30 km s^{-1} kpc^{-1}. From this pattern speed and the nuclear rotation curve inferred from our ^{13}CO (1–0) observations, we may tentatively identify an inner Lindblad resonance at radius $R \sim 13''$. This lies at the outer edge of the starburst and prominent molecular ridge. However, we note that the H I and ^{13}CO rotation curves are disjoint with different systemic velocities; proper determination of the ILR will hinge on recently acquired large-scale CO maps that will better link the kinematics of the disk and nucleus of this galaxy.

6. A MERGER-INDUCED STARBURST SCENARIO

6.1. *Evidence for Interaction*

Any scenario for the recent dynamical history of Maffei 2 must explain the basic observational properties of this galaxy, which include (1), a disrupted, asymmetric barred morphology, (2) an 11 km s^{-1} offset in systemic velocity between the disk and nucleus, and (3) the presence of a nuclear starburst. Such properties are characteristic of tidal interactions. We explore in this section the likelihood of an ongoing tidal interaction involving this galaxy.

While the basic morphology of Maffei 2 is that of a barred SBb galaxy, prominent distortions are evident in all available tracers of spiral structure. The asymmetries found in the radio continuum (§ 3) and H I (§ 4.1) are all the more striking because of their close correspondence with each

other (Fig. 5*b*) and with near-infrared images (Fig. 4*b*; Hurt et al. 1993a). In fact, the morphologies of the stellar distribution (near-infrared), star formation (radio continuum), and gas (including both H I and CO), are identical to at least first order. The asymmetries in Maffei 2 must therefore reflect some global disruption of the galaxy that has affected its overall structure. These primary features included a misaligned, asymmetrically defined bar and mismatched spiral arms. Similar features are commonly found in association with a forming bar in numerical simulations involving various geometries of galaxy interactions (Elmegreen et al. 1991; Hernquist et al. 1991; Hernquist & Mihos 1995).

Kinematic irregularities in the gas velocities also point toward a recent gravitational disruption. In particular, the 11 km s^{-1} offset in systemic velocity between the nuclear CO gas and the H I suggest that the galaxy is in a transient, nonequilibrium state. Likewise the asymmetries in the residual velocity field about the bar (§ 3.5) indicate that this galaxy is not rotating with a stable, antisymmetric velocity field as is seen in isolated barred galaxies.

The absence of more dramatic disruptions in the velocity field of Maffei 2 is not inconsistent with an interaction scenario. The observed velocity field is traced by H I gas, which in itself constitutes only a small fraction of the total dynamical mass. Even during interactions, save perhaps the most cataclysmic, a nondissipative galaxy halo will suffer only minor distortions. Since the halo dominates the gravitational potential at large radii, the gas kinematics should, to first order, reflect this potential. Gas kinematics causing disruptions in the morphology of the gas will to some extent represent second-order effects. This interpretation also applies to the velocity field of the gas in M51, which also shows little evidence of the obvious interaction with NGC 5195 (Tilanus et al. 1988); it is only in the outermost disk that bulk streaming motions become evident (Rots et al. 1990). A similar comparison may be made with NGC 1097, an SBbc barred galaxy with a circumnuclear ring of star formation. Its nearby companion NGC 1097A, a dwarf elliptical devoid of H I, has no obvious effect on the bulk internal kinematics of NGC 1097 despite its apparent proximity (Ondrechen et al. 1989).

In addition to causing morphological distortions that lead to the formation of bars, tidal interactions between galaxies are commonly believed to enhance nuclear star formation. The triggering mechanism for a starburst must be able to drive large quantities of gas into spatially confined regions. Steady state dissipation effects between offset gaseous and stellar bars can remove angular momentum from disk gas allowing it to flow into the nucleus. This effect is enhanced in tidal interactions and has been demonstrated in numerical simulations where prograde encounters between galaxies can cause the inflow or large quantities of gas to the nucleus, fostering enhanced star formation there (Barnes & Hernquist 1991; Hernquist 1989; Mihos, Richstone, & Bothun 1992). Tidal disruptions such as those between two large galaxies at close proximity can easily produce bars in otherwise axisymmetric galaxies (Elmegreen et al. 1991).

6.2. *A Merger Scenario for Maffei 2*

The possibility of a tidal interaction requires the presence of a companion galaxy. However, Maffei 2 appears to be relatively isolated in its environment. A recent near-infrared survey of the surrounding area found no evidence for any companion galaxies within a 20′ × 20′ square centered on the galaxy (Hurt, Levine, & Turner 1994). Its nearest known companion, the giant elliptical Maffei 1, is probably too distant (40′; 60 kpc) to account for the perturbations seen in Maffei 2 even if they lie at the same projected distance.

Simulations of encounters and mergers demonstrate that strongly asymmetric features tend to be relatively short-lived, blending out in relatively few rotational periods of the disk (Elmegreen et al. 1991; Mihos 1995; Hernquist & Mihos 1995). If the marked asymmetries in Maffei 2 have survived as many as two to three rotations of the outer optical disk, the encounter would have taken place within the last ~ 4–6×10^8 yr. This would imply relative velocities transverse to the line of sight of $V_{\rm trans} > 90$–130 km s^{-1} if Maffei 1 and 2 were to have interacted this "recently." The overall difference in velocity between the two galaxies would have to be much larger if they do not lie at exactly the same projected distance. Such large velocity dispersions can be found among members of large clusters but are less common for close companions. If one only needed to explain the triggering of a bar the constraints would be less severe, but in this argument we are specifically considering the significant north/south asymmetries. Nonetheless, we cannot rule out the possibility of a recent interaction between Maffei 1 and 2 producing the observed properties of the latter.

We propose, however, an alternate scenario to explain the morphological distortions and starburst of Maffei 2: an ongoing merger with a small companion galaxy. The possible culprit was first identified in near-infrared images by Hurt et al. (1993a) as a compact "blob" to the north of the nucleus, linked to the diffuse northern bar end by a diffuse "streamer." The proposed companion may be seen in the infrared image in Figure 4*b* (gray scale). In this star-subtracted H-band image, there is a bright, linear ridge $\sim 1\farcm5$ north of the northern end of the bar. Its approximate position is $\alpha_{1950} = 2^{\rm h}38^{\rm m}20\fs5$, $\delta_{1950} = 59°26'0''$, and it is approximately 1′ (1.5 kpc) in length at a position angle of $\sim 35°$, which aligns it very closely with the major axis. A fainter extension from this feature continues in the same direction for another full arcminute to the southwest; although it is difficult to make out in this figure it can be seen in a simultaneously-obtained *K*-band image, as well as a higher resolution *K*-band image (Mardones et al. 1996). It is interesting to note that in the 20 cm continuum map there is evidence for a corresponding linear ridge embedded in a more extended component of emission associated with the "streamer." It is difficult to understand how such an extensive, linear feature, which is oriented almost radially outward from the nucleus, could be dynamically maintained against differential rotation unless it were a recent, transient structure driven by a tidal interaction.

This companion is only the northernmost extent of the disruptions in this half of the galaxy. The radio continuum emission, which is an approximate tracer of star formation activity, is significantly enhanced in this half of the galaxy over the southern "normal" bar and spiral arm (there is $\sim 15\%$ more flux in equivalently sized regions in the north than in the south) despite the more diffuse extent and lack of ordered density wave found to the south. There are a number of H II regions in this area (H. Spinrad & L. Ho 1995, private communication), consistent with the picture of enhanced star formation due to tidal influence of the companion. The H I loops around in a "double arc" in this

region, turning back on itself at the location of the proposed companion; the continuum emission also loosely follows this feature (Fig. 5*b*). The outer H I arc is a significant structure, extending a full 3′ (4.4 kpc) in projection.

Recent simulation studies have demonstrated that mergers between disk galaxies and smaller satellite galaxies trigger morphological asymmetries and can likewise drive large quantities of gas into galactic nuclei to fuel starbursts (Mihos & Hernquist 1994; Hernquist & Mihos 1995). The morphology of such interactions is strikingly similar to that in Maffei 2. A typical time step from one of their simulations of a prograde satellite merger is presented in Figure 11. The left and right panels show the stellar and gas distributions, respectively. While not intended as a simulation of Maffei 2, the similarities are striking. The side of the galaxy associated with the satellite appears to be much more disrupted than the far side. The spiral arm trailing the satellite is longer and more diffuse in both stars and gas than the far arm, a situation very similar to that found in Maffei 2. The lack of gas on the side of the galaxy "leading" the companion in the simulation is also consistent with the observed H I asymmetry seen in Maffei 2. There is even a "double arc" of H I gas on the interacting side of the galaxy, with the companion spanning the two ridges of gas. This is again similar to what is seen in Maffei 2. Such "double arc" structures are also found in strongly interacting ocular galaxies (Elmegreen et al. 1991).

If the Maffei 2 starburst can be explained by an ongoing prograde merger with a satellite, why has it taken so long to notice this event? Interactions are easily identified from optical identifications, but in Maffei 2 the foreground extinction has interfered with observations in visible light. Very little of the galaxy's structure is evident in the plate of Spinrad et al. (1973). While near-infrared images of galaxies do not suffer as much from foreground extinction, they lack much of the contrast found in optical images and trace the diffuse base disk of cooler, fainter stars better than they trace the sharp features of dust lanes and the brightest, youngest stars (see, e.g., Rix & Rieke 1993). Combined with the expected tidal extrusion of the companion (which would further extend its brightness profile, making it less of a distinct stellar concentration) the dimmer contrast seen in Figure 4*b* is not unexpected. The overall H-band luminosity of the companion is significant accounting for ~4%–8% of the total luminosity of the galaxy (depending on how much of the northern tidal structure is taken to be associated with the companion). The mass of the companion in the merger simulation of Figure 11 was 10% of the galaxy mass (Mihos & Hernquist 1994); equating luminosity to mass as a first-order approximation, where therefore conclude there is sufficient mass in the Maffei 2 companion to drive the visible tidal asymmetries.

The northern companion does not, however, possess an independent kinematic signature in the H I velocity field. If it contained neutral gas itself, it would be expected to show independent signs of rotation. However, many dwarf elliptical galaxies contain little or no H I gas, so a rotation signature is not necessarily expected. Otherwise the H I gas kinematics will still be dominated by their response to the halo, with the tidal perturbations being a second-order effect. Such is the case in M51 where the H I velocity field is remarkably unperturbed for such an evident interaction; it is only near the gas-rich NGC 5195 that the field shows obvious distortions (Rots et al. 1990; Tilanus et al. 1988).

Although we have not ruled out the possibility of an earlier interaction with Maffei 1 triggering the nuclear starburst and generating the asymmetries in the galaxy, we feel that the merger scenario outlined above is more consistent with the visible morphology. This issue may possibly be resolved with large-field, deep optical imaging to better trace the younger, brighter stellar population. We note that this scenario implies that the starburst is still at a very young stage, since numerical simulations suggest the bulk of star formation lags the initial tidal encounter (Hernquist & Mihos 1995).

7. SUMMARY

We present high-resolution (20″; 480 pc) VLA H I and 21 cm continuum maps of the nearby spiral galaxy Maffei 2. The continuum morphology is very similar to the near-infrared (stellar) morphology, showing a central nuclear peak, a distinct bar, two asymmetric spiral arms, and a tidal feature to the north. These features are consistent with its identification as a peculiar barred spiral galaxy.

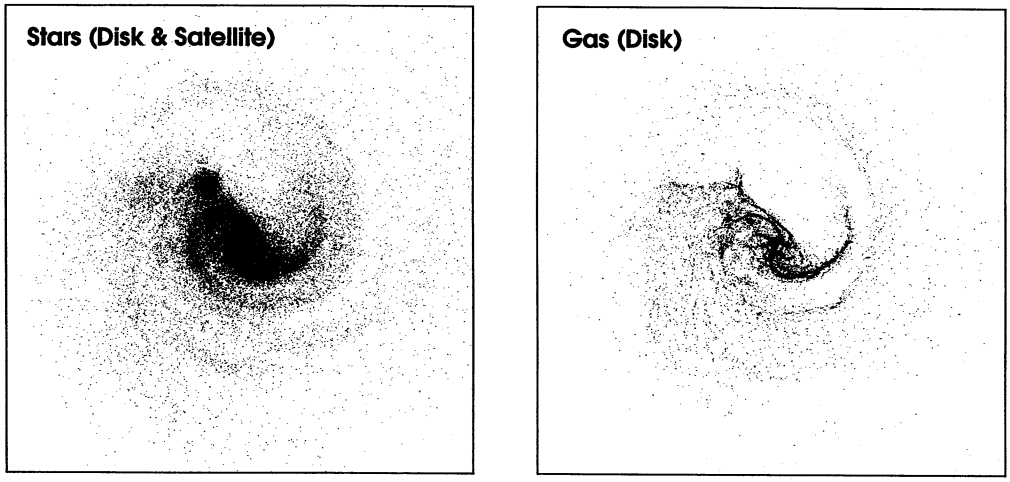

FIG. 11.—Simulation of satellite merger. These diagrams, kindly provided by Chris Mihos, illustrate a typical prograde merger of a small satellite galaxy with a disk galaxy. In this simulation (Mihos & Hernquist 1994) the satellite has 10% of the mass of the larger companion. The left panel shows the stellar distribution of the disk and satellite stars while the right shows the disk gas. Although not intended as an intentional model of the Maffei 2 system, it illustrates general morphological features of such a merger scenario.

Maffei 2 has a ringed H I morphology associated with two extended arms of gas. The inner H I hole is 2′ (3 kpc) in radius; the peak annulus of H I has an average column density of $\sim 1 \times 10^{21}$ cm^{-2}; this annulus is located at about 5 kpc from the center. The galaxy is markedly asymmetric in H I, with the 10^{20} cm^{-2} isophote extending 8′ (12 kpc) to the south, but only 4′ (6 kpc) to the north. The northern H I arm exhibits an unusual "double arc" structure. There exists very low column density (10^{19} cm^{-2}) H I emission to the north of the galaxy that has a significantly different position angle (0°) from the rest of the galaxy (−30°). The total H I mass in Maffei 2 is estimated to be 1.1×10^9 $M_\odot$, which is 1.5% of the total mass. This is toward the low end of the range for spirals.

In addition to the morphological peculiarities, there are also kinematic anomalies in Maffei 2. To first order the velocity field is circular, with strong noncircular radial streaming motions of ~ 50 km s^{-1} driven by the nonaxisymmetric potential of the stellar bar. The streaming motions across the arms are weaker in the north than in the south, consistent with the less well developed spiral structure in the north. The systemic velocity of the disk, traced by the H I, is offset by 10 km s^{-1} from that of the nucleus, traced by several independent observations of CO transitions.

Both the morphology and kinematics argue for a recent tidal interaction in Maffei 2 that has driven large quantities of gas into the nucleus to form the present starburst. While this could possibly be caused by a tidal interaction with the near-by elliptical Maffei 1, we propose that a more likely scenario is an ongoing prograde merger with a smaller satellite galaxy. Comparisons of the peculiar morphologies with numerical simulations of merging systems support this conclusion.

We extend effusive thanks to Chris Mihos for many insightful discussions and comments on this work. This research was supported in part by NSF grant NSF 9417968 and CalSpace grant CS 57-88.

REFERENCES

Allen, R. J., & Raimond, E. 1972, A&A, 19, 317
Bahcall, J. N., & Soniera, R. M. 1980, ApJS, 44, 73
Bania, T. M., & Lockman, F. J. 1984, ApJS, 54, 513
Barnes, J. E., & Hernquist, L. 1992, ARA&A, 30, 705
Bottinelli, L., Chamaraux, P., Gerard, E., Gouguenheim, L., Heidmann, J., Kazes, I., & Laugue, R. 1971, A&A, 12, 264
Brandt, J. C., & Scheer, L. S. 1965, AJ, 70, 471
Canzian, B. 1993, ApJ, 414, 487
Elmegreen, D. M., Sundin, M., Sundelius, B., & Elmegreen, B. 1991, A&A, 244, 52
England, M. N. 1989, ApJ, 337, 191
Giovanelli, R., & Haynes, M. P. 1988, in Galactic and Extragalactic Radio Astronomy ed. G. L. Verschuur & K. I. Kellerman (2d ed.; New York: Springer), 522
Gottesman, S. T., Ball, R., Hunter, J. H., Jr., & Huntley, J. M. 1984, ApJ, 286, 471
Hernquist, L. 1989, Nature, 340, 687
Hernquist, L., & Mihos, J. C. 1995, ApJ, 448, 41
Ho, P. T. P., Beck, S. C., & Turner, J. L. 1990, ApJ, 349, 57
Ho, P. T. P., Turner, J. L., Fazio, D. G., & Willner, S. P. 1989, ApJ, 344, 135
Huang, Z. P., Yin, Q.-F., Saslaw, W. C., & Heeschen, D. S. 1994, ApJ, 423, 614
Huchtmeier, W., Lercher, G., Seeberger, R., Saurer, W., & Weinberger, R. 1995, A&A, 293, 33
Hurt, R. L., Levine, D. A., & Turner, J. L. 1994, in Infrared Astronomy with Arrays: The Next Generation, ed. I. Maclean (Dordrecht: Kluwer), 175
Hurt, R. L., Merrill, K. M., Gatley, I., & Turner, J. L. 1993a, AJ, 105, 121
Hurt, R. L., & Turner, J. L. 1991, ApJ, 377, 434
Hurt, R. L., Turner, J. L., Ho, P. T. P., & Martin, R. N. 1993b, ApJ, 404, 602
Hurt, R. L., Turner, J. L., & Martin, R. N. 1996, in preparation
Kraan-Korteweg, R. C., Loan, A. J., Burton, W. B., Lahav, O., Ferguson, H. C., Henning, P. A., & Lynden-Bell, D. 1994, Nature, 372, 77
Maffei, P. 1968, PASP, 80, 618
Mardones, D., Fazio, G. G., Willner, S. P., Peletier, R., & Rieke, M. 1996, in preparation
Mathewson, D. S., van der Kruit, P. C., & Brouw, W. N. 1972, A&A, 17, 468
McCall, M. L., & Buta, R. J. 1995, AJ, 109, 2460
Mihos, J. C. 1995, ApJ, 438, 75L
Mihos, J. C., & Hernquist, L. 1994, ApJ, 431, 13L
Mihos, J. C., Richstone, D. O., & Bothun, G. D. 1992, ApJ, 400, 153
Ondrechen, M. P. 1985, AJ, 90, 1474
Ondrechen, M. P., & van der Hulst, J. M. 1989, ApJ, 342, 29
Ondrechen, M. P., van der Hulst, J. M., & Hummel, E. 1989, ApJ, 342, 39
Rickard, L. J., & Harvey, P. M. 1983, ApJ, 268, L7
———. 1984, P. M. 1983, ApJ, 268, 1520
Rix, H.-W., & Rieke, M. J. 1993, ApJ, 418, 123
Roberts, M. S. 1969, AJ, 74, 859
Roberts, W. W., Huntley, J. M., & van Albada, G. D. 1979, ApJ, 233, 67
Rots, A. H., Bosma, A., van der Hulst, J. M., Athanassoula, E., & Crane, P. C. 1990, AJ, 100, 387
Seaquist, E. R., Pfund, J., & Bignell, R. C. 1976, A&A, 48, 413
Shostak, G. S., & Weliachew, L. 1971, ApJ, 169, L71
Spinrad, H. 1995, private communication
Spinrad, H., et al. 1971, ApJ, 163, L25
———. 1973, ApJ, 180, 351
Telesco, C. M., Dressel, L. L., & Wolstencroft, R. D. 1993, ApJ, 414, 120
Tilanus, R. P., & Allen, R. J. 1991, A&A, 244, 8
Tilanus, R. P. J., Allen, R. J., van der Hulst, J. M., Crane, P. C., & Kennicutt, R. C. 1988, ApJ, 330, 667
Turner, J. L., & Ho, P. T. P. 1994, ApJ, 421, 122
Weaver, H., & Williams, D. R. W. 1973, A&AS, 8, 1
———. 1974, A&AS, 17, 1
Weiler, K. W., Sramek, R. A., Panagia, N., van der Hulst, J. M., & Salvati, M. 1986, ApJ, 301, 790
Wright, M. C. H. 1974, in Galactic and Extragalactic Radio Astronomy, ed. G. L. Verschuur & K. I. Kellerman (1st ed.; New York: Springer), 291
Wright, M. C. H., & Seielstad, G. A. 1973, Astrophys. Lett., 13, 1